Stellar Overdensity in the Local Arm in *Gaia* DR2

Yusuke Miyachi[1], Nobuyuki Sakai[2,3], Daisuke Kawata[4], Junichi Baba[5], Mareki Honma[2,6,7], Noriyuki Matsunaga[8], and Kenta Fujisawa[1]

[1] Department of Physics, Faculty of Science, Yamaguchi University, Yoshida 1677-1, Yamaguchi-city, Yamaguchi 753-8512, Japan
[2] Mizusawa VLBI observatory, National Astronomical Observatory of Japan, 2-21-1 Osawa, Mitaka, Tokyo 181-8588, Japan
[3] Korea Astronomy & Space Science Institute, 776, Daedeokdae-ro, Yuseong-gu, Daejeon 34055, Republic of Korea
[4] Mullard Space Science Laboratory, University College London, Holmbury St. Mary, Dorking, Surrey RH5 6NT, UK
[5] National Astronomical Observatory of Japan, 2-21-1 Osawa, Mitaka, Tokyo 181-8588, Japan
[6] Mizusawa VLBI observatory, National Astronomical Observatory of Japan, 2-12 Hoshi-ga-oka-cho, Mizusawa-ku, Oshu, Iwate 023-0861, Japan
[7] The Graduate University for Advanced Studies (Sokendai), Mitaka, Tokyo 181-8588, Japan
[8] Department of Astronomy, The University of Tokyo, 7-3-1 Hongo, Bunkyo-ku, Tokyo 113-0033, Japan

Abstract

Using the cross-matched data of *Gaia* DR2 and the 2MASS Point Source Catalog, we investigated the surface density distribution of stars aged ~ 1 Gyr in the thin disk in the range of $90° \leqslant l \leqslant 270°$. We selected 4654 stars above the turnoff corresponding to the age ~ 1 Gyr, that fall within a small box region in the color–magnitude diagram, $(J - K_s)_0$ versus $M(K_s)$, for which the distance and reddening are corrected. The selected sample shows an arm-like overdensity at $90° \leqslant l \leqslant 190°$. This overdensity is located close to the Local Arm traced by high-mass star-forming regions (HMSFRs), but its pitch angle is slightly larger than that of the HMSFR-defined arm. Although the significance of the overdensity we report is marginal, its structure poses questions concerning both of the competing scenarios of spiral arms, the density-wave theory, and the dynamic spiral arm model. The offset between the arms traced by stars and HMSFRs, i.e., gas, is difficult to explain using the dynamic arm scenario. On the other hand, the pitch angle of the stellar Local Arm, if confirmed, is larger than that of the Perseus arm, and is difficult to explain using the classical density-wave scenario. The dynamic arm scenario can explain the pitch angle of the stellar Local Arm, if the Local Arm is in a growing up phase, while the Perseus arm is in a disrupting phase. Our result provide a new and complex picture of the Galactic spiral arms, and encourages further studies.

Key words: Galaxy: disk – Galaxy: kinematics and dynamics – Galaxy: structure – solar neighborhood

1. Introduction

Revealing the shapes of spiral arms in the Milky Way is a long-standing challenge in Galactic astronomy (e.g., Vallée 2017). The first successful identification of spiral arms in the Milky Way was made by Morgan et al. (1952) from distributions of ionized hydrogen in the solar neighborhood. Since then, many studies have reported the characteristics of spiral arms in the Milky Way (e.g., van de Hulst et al. 1954; Oort et al. 1958; Georgelin & Georgelin 1976; Russeil 2003; Paladini et al. 2004; Hou & Han 2014). The well-known spiral arms within a few kiloparsecs of the Sun are the Sagittarius–Carina arm and the Perseus arm. The Sagittarius–Carina arm passes Galactic longitude of $l = 0°$ inside the solar radius, and the Perseus arm passes $l = 180°$ outside the solar radius. These features are revealed by a large number of gas and young stellar tracers, such as O and early B stars, giant molecular clouds, and H_{II} regions (Bok et al. 1970; Russeil 2003; Hou et al. 2009; Hou & Han 2014; Monguió et al. 2015). The Perseus arm is also associated with the excess of older stars (Churchwell et al. 2009, and references therein). On the other hand, such an excess of old stars has not been found around the Sagittarius arm (Benjamin et al. 2005). This leads to an ongoing debate that the Perseus arm could be one of two major spiral arms in the Milky Way, while the Sagittarius–Carina arm is a minor gaseous spiral arm (Drimmel 2000; Benjamin 2008;

Churchwell et al. 2009). Spiral patterns in the Galactic plane are also traced by high-mass star-forming regions (HMSFRs) whose precise parallaxes can be measured using Very Long Baseline Interferometry (Reid et al. 2009; Honma et al. 2012; Reid & Honma 2014). More than 100 HMSFRs have been identified at the expected locations of the Sagittarius–Carina and Perseus arms (Reid et al. 2014).

There is another spiral arm between the Sagittarius–Carina and Perseus arms, called the "Local Arm" or the "Orion Arm" (van de Hulst et al. 1954; Georgelin & Georgelin 1976; Reid et al. 2014; Xu et al. 2016). The Local Arm is identified by neutral hydrogen gas, H_{II} regions, Cepheids, OB stars, and HMSFRs (Walraven et al. 1958; Bok 1959; Becker & Fenkart 1970; Hou & Han 2014; Xu et al. 2016, 2018a), however, the features of the Local Arm are not very clear, compared to the Sagittarius–Carina and Perseus arms. The Local Arm is often considered to be a branch-like features or a spur which bridges between the Sagittarius–Carina arm and the Perseus arm (Oort & Muller 1952; Morgan et al. 1953; van de Hulst et al. 1954; Kerr 1970; Kerr & Kerr 1970; Russeil 2003; Russeil et al. 2007; Xu et al. 2016, 2018a). This infers that the Local Arm is not a major spiral arm, but a secondary minor spiral feature, which connects patchy star-forming regions that are only traced by gas and very young stars (Gum 1955; Bok 1959; Bok et al. 1970; Kerr 1970; Georgelin & Georgelin 1976; Hou & Han 2014). A large number of HMSFRs are observed in the Local Arm, and the overall length (>5 kpc) identified with HMSFRs is substantial, which led to a recent debate that the Local Arm may be a major spiral arm (Xu et al. 2013, 2016). If the Local Arm is a major spiral arm, we

should be able to identify the stellar overdensity of the Local Arm, which has not been observed, despite it being the closest spiral arm.

The European Space Agency's *Gaia* mission (Gaia Collaboration et al. 2016) has made their second data release (Gaia DR2; Gaia Collaboration et al. 2018). Gaia DR2 provides the position, parallax and proper motions for $\sim 1.3 \times 10^9$ stars in the Milky Way (Lindegren et al. 2018), and radial velocity for about 7 million stars (Soubiran et al. 2018) measured using a Radial Velocity Spectrograph (Cropper et al. 2018). The precise measurement of the parallax for the bright stars around the Local Arm in *Gaia* DR2 enables us to study the stellar distribution for a selected population of stars. In this paper, to answer the question of whether or not there is a stellar arm associated with the Local Arm, we map the stellar density of a specific population of stars with about 1 Gyr of age at $90 < l < 270°$. The 1 Gyr population is chosen, because they are significantly older than the previously known Local Arm tracers, and they are bright and more uniquely located in the Hertzsprung–Russell (HR) diagram. Cross-matched samples of Gaia DR2 stars with the Two Micron All Sky Survey Point Source Catalog (2MASS PSC; Skrutskie et al. 2006) are used to identify the population of the stars. We also evaluated the completeness of our selected sample against the 2MASS PSC, and confirmed that our sample has reasonable completeness within the distance of 0.2 and 1.3 kpc.

If the stellar arm is identified, and therefore, the positional offset between the gas and stellar arms, it would be interesting to consider the origin of the spiral arm (Dobbs & Pringle 2010; Baba et al. 2015; Egusa et al. 2017). Recently, the origin of the spiral arm is hotly debated. There are two major competing scenarios for isolated spiral galaxies (see a review by Dobbs & Baba 2014): one of them is a classic density-wave scenario, where the spiral arm is considered to be long-lived and have rigidly rotating density wave features (Lin & Shu 1964, 1966; Bertin & Lin 1996), the other one is a transient dynamic spiral arm scenario, which is commonly seen in *N*-body simulations of disk galaxies. In the latter scenario, the spiral arm is short-lived, transient, and recurrent (Sellwood & Carlberg 1984; Fujii et al. 2011; D'Onghia et al. 2013), and the arm is co-rotating and winding with the stars at every radius (Wada et al. 2011; Grand et al. 2012a; Baba et al. 2013). This is also the case for barred spiral galaxy simulations (Baba et al. 2009; Grand et al. 2012b; Baba 2015). In the density-wave scenario, the stellar arm is expected to have different degrees of offset from the gas arm at different radii (e.g., Fujimoto 1968; Roberts 1969; Gittins & Clarke 2004), and hence the gas and spiral arms have different pitch angles (e.g., Pour-Imani et al. 2016). On the other hand, the dynamic spiral arm scenario predicts no systematic offset of the gas and stellar arms, because they are co-rotating with each other (Grand et al. 2012a; Kawata et al. 2014; Baba et al. 2015).

This paper investigates the stellar overdensity in the Local Arm and the offset of the stellar arm from the gas arm identified with the HMSFRs. Section 2 describes our selection of the 1 Gyr age stellar population and discusses the distance range where the selected population shows reasonable completeness. Section 3 shows our results. Summary and discussion are provided in Section 4.

2. Data

The data used in this paper are described in this section. We first explain how we selected our sample of stars to analyze the surface stellar density map around the Local Arm in Section 2.1. Then, in Section 2.2 we describe the maser sources associated with HMSFRs, which are used to define the location of the Local Arm for the star-forming regions, i.e., gas. We assumed the solar radius of $R_0 = 8.34$ kpc (Reid et al. 2014) in this paper.

2.1. Stellar Data

In this paper we focus on the stellar population with an age of around 1 Gyr, and measure the surface density map to test if there is any stellar overdensity in the Local Arm. Although the age of 1 Gyr is a relatively young age, the stellar populations are older than the populations previously used to identify the Local Arm, and we consider that they are old enough to represent the stellar mass distribution of the Galactic thin disk stars. Also, the relatively young stellar population was chosen because the color and magnitude ranges of their turn-off stars are more isolated in the HR diagram. In this paper, we focus on the region of the Galactic longitude between $l = 90°$ and $l = 270°$, because the dust extinction is less severe, and a clear excess of the HMSFRs is observed and identified as the Local Arm (Reid et al. 2014), in this longitude range. We select the 1 Gyr stellar population from the HR diagram in near-infrared, to minimize the dust extinction. We cross-matched Gaia DR2 with the 2MASS PSC (Skrutskie et al. 2006), using the official *Gaia* DR2-2MASS cross-match best neighbor table (Marrese et al. 2019). For the 2MASS PSC (Skrutskie et al. 2006) we select the sample whose near-infrared photometric quality flag of K_s band is at least "A," which means, the scan signal to noise ratio is greater than 10. Bennett & Bovy (2019) argues that the Gaia DR2-2MASS cross-matched sample is complete within $7 < G < 17$ mag with conservative estimates. Following their approach, we select the Gaia DR2 sample within $7 < G < 17$ mag. The total number of this sample is 39,253,853 (Gaia DR2-2MASS sample).

From the Gaia DR2-2MASS sample, we further select stars that have an accurate measurement of the parallax available in Gaia DR2 (Gaia Collaboration et al. 2018) with a relative parallax uncertainty of $\pi/\sigma_\pi > 5$ (where π and σ_π are the parallax, and its uncertainty, respectively). As we are interested in the surface density of the disk stars, we select stars within $|z| < 0.3$ kpc, where $|z|$ is defined as a vertical position with respect to the Sun's vertical position, $z_\odot$. When we evaluate $|z|$, we simply assume $d = 1/\pi$ without taking into account the uncertainty in parallax. To estimate the three-dimensional Galactic dust extinction correction, we employ MWDUST[9] (Bovy et al. 2016). This allows us to obtain extinction corrected color, $(J - K_s)_0$, and absolute magnitude, M_{Ks}, i.e., the HR diagram as shown in Figure 1.

We then select the stars within $0.1 \leqslant (J - K_s)_0 \leqslant 0.2$ and $0.0 \leqslant M_{Ks} \leqslant 0.3$ in the HR diagram as our sample for 1 Gyr stellar population, which leaves 33,718 stars. This region in the HR diagram corresponds to the box area highlighted in Figure 1. Figure 1 also shows the track of PARSEC+COLIBRI isochrones (Bressan et al. 2012; Marigo et al. 2017) with ages of 1 and 1.5 Gyr with the solar metallicity ($Z_\odot = 0.0152$) and a
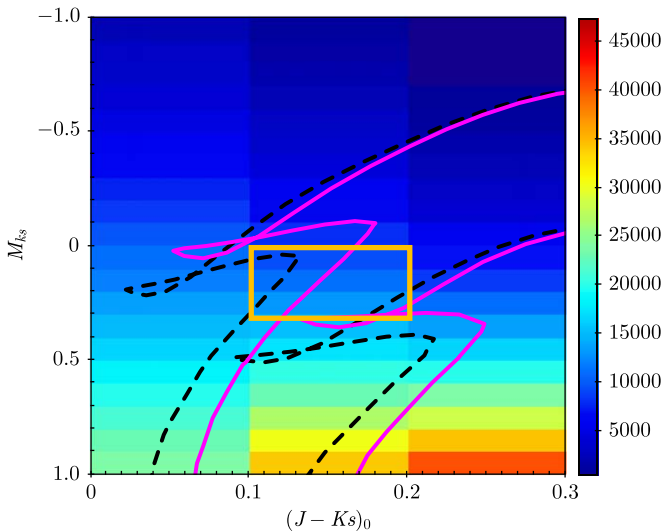
---

[9] https://github.com/jobovy/mwdust

Figure 1. Color–magnitude distribution of M_{K_s} vs. $(J - K_s)_0$ for our sample after cross-matching *Gaia* DR2 and 2MASS data. The bin size is 0.1×0.1 mag and the color indicates the number of stars per bin as shown with the color bar on the right. The left and right magenta (black dashed) lines indicate the PARSEC+COLIBRI isochrone with an age of 1 and 1.5 Gyr, respectively, with the solar metallicity (a metallicity of $Z = 0.0096$). The solid box represents the color–magnitude ranges for selecting our 1 Gyr age population.

Figure 2. The estimated K_s-band extinction, A_{K_s} for our selected stars as a function of the distance, d. The color indicates the number of sources per bin as indicated in the color bar on the right. The red horizontal dotted lines indicate $A_{K_s} = 0.6$ mag.

lower metallicity of $Z = 0.0096$. The figure indicates that our selected region in the HR diagram corresponds to turn-off stars with an age of between about 1 and 1.5 Gyr with the metallicity expected in the disk stars outside of the solar radius, where we focus on in this paper. There could be some contamination of blue horizontal branch stars of the Galactic halo stars in this color and magnitude range. We analyzed the vertical distribution of our selected stars, and confirmed that they are mostly confined within $|z| < 0.2$ kpc. We also confirmed that the stellar density drops rapidly with $|z|$. Hence, we consider that in the volume we study in this paper, the thin disk stars are dominant, and the contamination of the blue horizontal branch stars is negligible.

We found that our sample is estimated to be complete in an acceptably high level within $0.2 \leqslant d \leqslant 1.33$ kpc. This corresponds to the projected distance in the disk plane, d_{xy}, of $0.2 < d_{xy} < 1.3$ kpc, when the sample is limited within $|z| < 0.3$ kpc as mentioned above. We exclude the stars within $d_{xy} < 0.2$ kpc, because Gaia DR2 is incomplete for nearby bright stars with $G < 7$ mag. We also exclude the stars at $d_{xy} > 1.3$ kpc, because the completeness drops at the farther distance. Hence, our final sample used in this paper is limited within $0.2 < d_{xy} < 1.3$ kpc and $|z| < 0.3$ kpc, producing a final sample of 4654 stars.

We evaluated that our sample is complete in an acceptably high level within the distance (d) between 0.2 and 1.33 kpc as follows. Figure 2 shows the extinction, A_{K_s}, in our selected Galactic longitude region, i.e., $90° \leqslant l \leqslant 270°$, within $|z| < 0.3$ kpc from the Sun, and the distance within $0.2 \leqslant d \leqslant 1.33$ kpc, using MWDUST. We found that almost all the sample have $A_{K_s} < 0.6$ mag. Our sampled absolute magnitude range of $0.0 \leqslant M_{K_s} \leqslant 0.3$ mag corresponds to $6.5 \leqslant K_s \leqslant 11.5$ mag at $0.2 \leqslant d \leqslant 1.33$ kpc with the maximum extinction of $A_{K_s} < 0.6$ mag. The brightest limit of 6.5 mag corresponds to the apparent magnitude of $M_{K_s} = 0$ mag at the minimum distance of $d = 0.2$ kpc and the faintest limit corresponds to the apparent magnitude of $M_{K_s} = 0.3$ mag at $d = 1.33$ kpc plus the maximum extinction of $A_{K_s} = 0.6$ mag. We found that our sample within the square region of
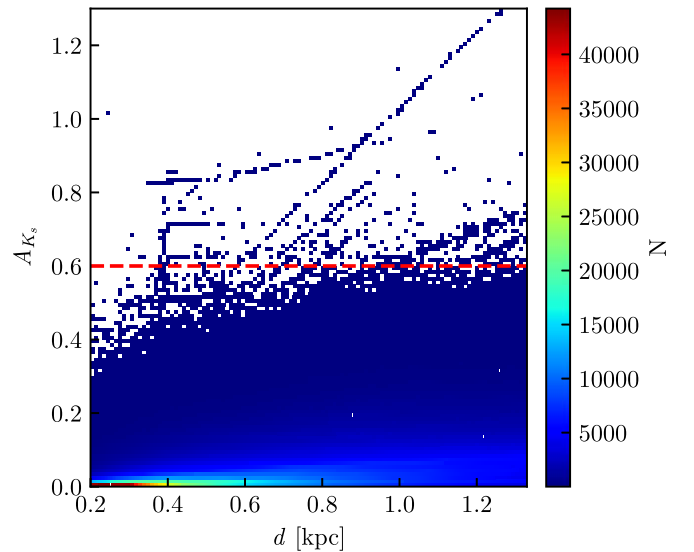
Figure 1, i.e., $0.1 \leqslant (J - K_s)_0 \leqslant 0.2$ mag and $0.0 \leqslant M_{K_s} \leqslant 0.3$ mag, are within $0.5 < G - K_s < 5.5$. This means that for our sample $6.5 \leqslant K_s \leqslant 11.5$ mag corresponds to $7 < G < 17$ mag. As discussed above, according to Bennett & Bovy (2019) the Gaia DR2-2MASS cross-matched sample is complete within $7 < G < 17$ mag.

However, our final sample is additionally limited to the stars with $\pi/\sigma_\pi > 5$, therefore, we compare our final sample with the Gaia DR2-2MASS sample in our selected volume and color–magnitude range. To this end, we made a comparison sample, Group C, from the Gaia DR2-2MASS sample, which has $7 < G < 17$ mag cut, by selecting the stars within $0.1 \leqslant (J - K_s)_0 \leqslant 0.2$ mag, $0.0 \leqslant M_{K_s} \leqslant 0.3$ mag, $|z| < 0.3$ kpc and $0.2 < d_{xy} < 1.33$ kpc, using their distance of $d = 1/\pi$, regardless of their uncertainty. Parallax uncertainties of Group C can be large, therefore, there is contamination from the stars whose true distance, absolute magnitude or color is not within the selected range. Group C must be missing some stars whose true distance, color and magnitude are within the selected range of our final sample, but not in Group C, because of their error in parallax. Here, we consider that these can compensate for each other to some degree, and Group C is close to being a reasonable representative complete sample to be compared with our final sample for simplicity. We obtain 4798 stars in Group C and 4654 stars satisfy $\pi/\sigma_\pi > 5$. This leads to 97% of stars in Group C being in our final sample, and the additional cut of $\pi/\sigma_\pi > 5$ does not reduce the sample fraction significantly. Hence, our final sample is considered to be a reasonably representative sample to estimate the density distribution of our selected population of stars.

Note that here we use the cataloged values of parallax, color and magnitude in Gaia DR2 and 2MASS without taking into account the uncertainty. In addition, 3D dust extinction is still uncertain even in an area relatively near the Sun, but we simply use mwdust to correct the dust extinction, for simplicity. The errors in these measurements and uncertainties in the dust extinction affect which stars are included in our color–magnitude range or within the chosen spatial range of distance and height.
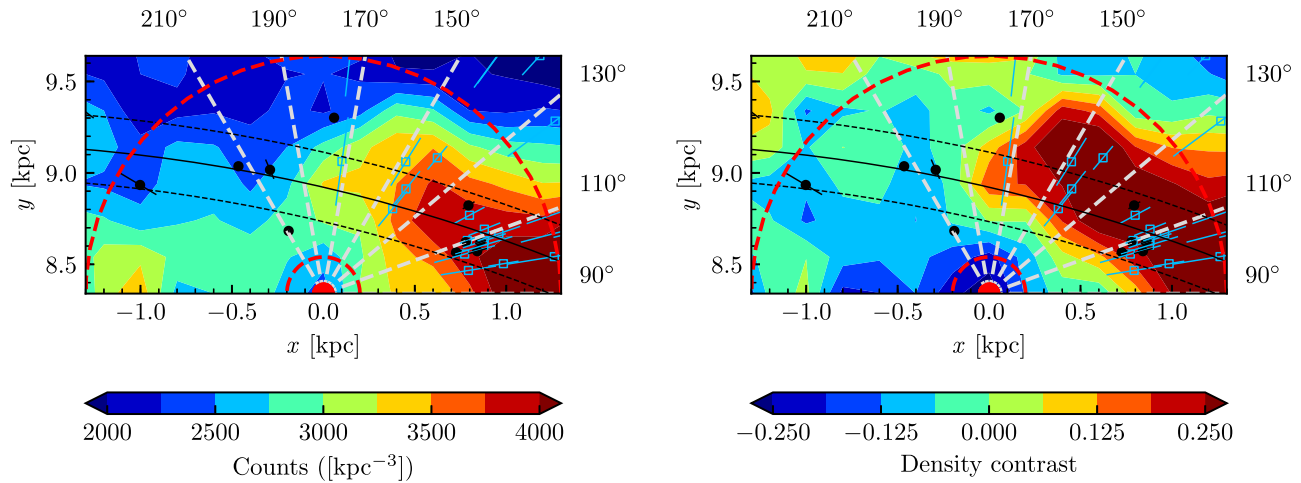
Figure 3. The smoothed density distribution of our selected stars as 1 Gyr stellar populations (Left) and the distribution after division by an exponential profile with the scale length $r_d = 2.5$ kpc (e.g., Bland-Hawthorn & Gerhard 2016) (Right). The Sun is located at $(x, y) = (0, 8.34)$ kpc. The x-axis is the direction of the Galactic rotation, and the y-axis is the direction from the Galactic center to the Sun. The location of the Local Arm defined with HMSFRs is highlighted by a solid black line and the dashed black lines indicate the width of the arm defined in Section 2.2. The inner and outer dashed red lines correspond to the distances from the Sun $d_{xy} = 0.2$ and 1.3 kpc, and we consider that the completeness of our sample is reasonably high in the area between these lines (see Section 2.1). Filled black circles with error bars show the location of the HMSFRs, and the error bars correspond to the distance uncertainties. Open blue squares with error bars indicate the locations of H$_{II}$ regions in $90° \leqslant l \leqslant 190°$ from Foster & Brunt (2015).

In this paper, we assume that the errors affect both the increase and decrease of the sample compared to the true sample, however, these compensate for each other, and the final results are less affected by the uncertainties. Still, more statistical tests are required to properly assess the effects of these errors. We postpone such statistical study to a future paper, but this paper provides more qualitative indications from the selected sample which are chosen to be a representative sample for our selected stellar population.

2.2. High Mass Star-forming Regions and The Local Arm

As discussed in Section 1, the Local Arm is currently identified by the star-forming regions, young OB stars and young open clusters (e.g., Xu et al. 2018a). To define the location of the Local Arm where the stars are forming, we use HMSFRs as shown in Xu et al. (2016), to compare the stellar density distribution from our selected Gaia DR2 stars in the previous section. To define the location of the Local Arm from the star-forming regions, using the model described in Reid et al. (2014), we fit the distribution of HMSFRs with a following logarithmic spiral-arm model,

$$\ln(R/R_{\rm ref}) = -(\beta - \beta_{\rm ref})\tan\psi, \qquad (1)$$

where $R_{\rm ref}$ is a reference Galactocentric radius, $\beta_{\rm ref}$ is a reference azimuthal angle and ψ is a pitch angle. The zero-point of the Galactocentric azimuthal angle, β, is defined as a line toward the Sun from the Galactic center, and the angle increases toward the direction of the Galactic rotation. $\beta_{\rm ref}$ was set near the midpoint of the azimuthal angles for the Local Arm HMSFR sources in Xu et al. (2016).

As we focus on the stellar density distribution in the second and third Galactic quadrants ($90° \leqslant l \leqslant 270°$), we apply the fitting with Equation (1) to the 12 Local Arm HMSFR sources within $90° \leqslant l \leqslant 270°$. Then, we obtain $(R_{\rm ref}, \beta_{\rm ref}) = (8.87 \pm 0.13$ kpc, $1°.4)$, and $\psi = 13°.1 \pm 7°.5$. The arm's width, a_w, defined as the 1σ scatter in the sources perpendicular to the fitted arm position, is 0.19 kpc. The location of the Local Arm

identified with HMSFRs (HMSFR-defined Local Arm, hereafter) is shown with the solid line in Figure 3, and the dashed lines show the width of the arm. Note that two HMSFRs are outside of the region shown in Figure 3, where only 10 HMSFRs can be seen. Also note that this location of the HMSFR-defined Local Arm is different and has a significantly larger pitch angle than the Local Arm identified in Xu et al. (2016), because Xu et al. (2016) included the Local Arm HMSFRs sources in the lower Galactic longitude, $70° \leqslant l \leqslant 270°$. Our results provide a better fit in the region that we are interested in. The spiral arm may be segmented and different parts of the arm may have different pitch angles (e.g., Honig & Reid 2015), therefore, we use our new fit of the HMSFR-defined Local Arm in the region of our interest in this paper.

Xu et al. (2016, 2018a, 2018b) identified a minor segment situated between the Local and the Sagittarius arms in the first quadrant. We confirmed that the extrapolation of the minor segment does not come close to the HMSFR-defined Local Arm. Hence, we do not consider that the minor segment is related to the HMSFR-defined Local Arm in the region we focus on in this paper.

3. Results

Using the sample of stars selected as the 1 Gyr old population, described in Section 2.1, we analyzed the surface density distribution of 1 Gyr old stars. The smoothed surface density distribution is shown in the left panel of Figure 3. Here, we define the x-axis as a direction of the rotation from the Sun with the Sun's location at $x = 0$ kpc, and the y-axis is the direction from the Galactic center to the Sun whose location is $y = r_0 = 8.34$ kpc. The red inner and outer dashed half-circles indicate the distance from the Sun of $d_{xy} = 0.2$ and 1.3 kpc, respectively. As discussed in Section 2.1, the completeness of our sample drops rapidly inside the inner red dashed circle or outside the outer red dashed circle. Hence, we trust the density map only between these two red dashed half-circles. The solid line shows the location of the Local Arm defined with the HMSFR-defined Local Arm in Section 2.2. Interestingly, there

is a clear stellar overdensity of the 1 Gyr old stars at a similar location to the HMSFR-defined Local Arm at $90° \leqslant l \leqslant 190°$, or slightly outside of the HMSFR-defined Local Arm at a larger Galactic longitude at $l \geqslant 130°$. The most significant stellar overdensity is seen between $l = 90°$ and $l = 110°$. The stellar overdensity looks extended along the HMSFR-defined Local Arm from $l = 90°$ to $l = 190°$, at least. In a region larger than that of the Galactic longitude $l = 190°$, although there are HMSFRs, and the HMSFR-defined Local Arms extend continuously as shown in the black solid line and the dashed lines, the extension of the stellar overdensity is not clear within our distance limit.

To take into account the mean stellar density decrease with the increasing Galactocentric radius, the right panel of Figure 3 shows the smoothed density distribution of 1 Gyr stars after division by an exponential density profile with the scale length of $r_d = 2.5$ kpc (e.g., Bland-Hawthorn & Gerhard 2016). The arm-like structure of the stellar overdensity in $90° \leqslant l \leqslant 190°$ as seen in the left panel of Figure 3 still exists after taking into account the decrease in the stellar density at the outer radii.

To quantify the significance of this overdensity, we compute the stellar density after division by the exponential law as a function of the distance from the Sun in the different longitudinal regions between $l = 90°$ and $l = 210°$. The results are shown in Figure 4. We evaluate the uncertainty of the density in each distance bin by taking the dispersion of the density in each bin measured from 500 bootstrap realization of the sample. Within $90° \leqslant l \leqslant 110°$ the stellar density increases with the distance from the Sun, and the density peak is seen at close to our distance limit of $d_{xy} = 1.3$ kpc, as seen in Figure 3. Although it is not very clear at $110° \leqslant l \leqslant 130°$, at $130° \leqslant l \leqslant 190°$, we can see a clearer peak of density within our distance limit, and the density decreases with the increasing distance after passing the density peak. This peak corresponds to the arm-like overdensity seen in Figure 3, and the significance of the overdensity is about 2σ, when comparing the highest density peak and the uncertainty, especially at $130° \leqslant l \leqslant 170°$. Hence, we think that the stellar overdensity seen in Figure 3 is very likely a real structure.

Figure 4 also confirms that at $l \geqslant 190°$ the overdensity is not very clear. The histograms of the density distribution as a function of distance in $190° \leqslant l \leqslant 210°$ show a hint of the overdensity, but it is not statistically significant. Hence, as seen in Figure 3, at $l \geqslant 190°$ there is no significant stellar component that corresponds to the HMSFR-defined Local Arm or they are farther than the distance that we can confidently analyze the stellar density.

The vertical gray area in Figure 4 shows the distance range of the HMSFR-defined Local Arm in the corresponding Galactic longitude range in each panel. Interestingly, at $130° \leqslant l \leqslant 190°$ the location of the stellar Local Arm overdensity is slightly outside of the HMSFR-defined Local Arm at a larger Galactic longitude. On the other hand, at lower Galactic longitude, $110° \leqslant l \leqslant 130°$ the HMSFR-defined Local Arm is located at the center of the stellar overdensity, although the width of the arm overdensity is not very clear. This trend is also seen in the right panel of Figure 3. If this is true, the stellar Local Arm we identified has a slightly larger pitch angle than the HMSFR-defined Local Arm. We will discuss the implication of this result in Section 4.

4. Summary and Discussion

Taking advantage of the precise measurements of parallax for a large number of stars recently provided by *Gaia* DR2, we analyzed a surface stellar density map for a relatively old ($\sim$1 Gyr) stellar population of the thin disk stars between $90° \leqslant l \leqslant 270°$. We identified the 1 Gyr population from a carefully chosen range of the color and magnitude in the near-infrared bands, after cross-matching Gaia DR2 and 2MASS. We evaluated that our sample is reasonably complete within the distance between 0.2 and 1.3 kpc. We found a marginally significant arm-like stellar overdensity close to the Local Arm, identified with the HMSFRs especially in the region of $90° \leqslant l \leqslant 190°$. At $l \geqslant 190°$ we could not find a significant stellar overdensity. At $90° \leqslant l \leqslant 190°$ the identified stellar Local Arm is located in a similar region to the HMSFR-defined Local Arm. Our findings indicate that the Local Arm is not a minor arm with only the gas and star-forming clouds, but a significant stellar overdensity is also associated.

Interestingly, at $130° \leqslant l \leqslant 190°$, the identified stellar Local Arm is located slightly outside of the HMSFR-defined Local Arm, while at lower Galactic longitude of $90° \leqslant l \leqslant 130°$, the stellar Local Arm is co-located with the HMSFR-defined Local Arm. This indicates that the pitch angle of the stellar arm is slightly larger than the HMSFR-defined arm, and there is an offset between HMSFR-defined (i.e., gas) and stellar arms, especially at the larger Galactic longitude, $130° \leqslant l \leqslant 190°$. The offset and different pitch angles between the stellar and gas spiral arms are consistent with what is expected from a classical density-wave and its galactic shock theory (e.g., Roberts 1969). Hydrodynamic simulations with the rigidly rotating spiral arm potentials also consistently show that the pitch angle of the gas arm is smaller than that of the (stellar) spiral arm (Gittins & Clarke 2004; Baba et al. 2015). However, we note that the pitch angle of the stellar Local Arm is larger compared to the other major spiral arms like the Perseus arm and the Scutum-Centaurus arm (e.g., Reid et al. 2014). This could be an issue for a classical density-wave theory where a constant pitch angle is expected in the different spiral arms, at least at the same radius. More complicatedly, Vallée (2018) found an offset between the CO arm, and the HMSFR-defined arm, in the Perseus arm, where the CO spiral arm (earlier phase of gas spiral arm) shows a larger pitch angle than the HMSFR-defined spiral arm. How this can be compared with the offset between the stellar arm and the HMSFR-defined arm is not a trivial question and Pour-Imani et al. (2016) argues that there are two scenarios of the offset of stellar and gas spiral arms in the density-wave scenario. It is required to further study the offset between different arm tracers in the different spiral arms in the Milky Way. Clearer theoretical predictions in the density-wave scenario are also necessary.

In Figure 3, we also show the locations of the H$_{II}$ regions from Foster & Brunt (2015) who measured the distance to the H$_{II}$ regions within $90° \leqslant l \leqslant 190°$. The H$_{II}$ regions are also located in the similar region to the stellar overdensity we identified. Interestingly, the right panel of Figure 3, which shows the stellar overdensity after taking into account the mean stellar density decrease with the increasing Galactocentric radius, tentatively shows that the H$_{II}$ regions seem to be located between the identified stellar arm and the HMSFR-defined Local Arm. Admittedly, this is a tentative trend with very low number statistics. However, if this is confirmed, because the H$_{II}$ regions are considered to be the star formation tracer phase later
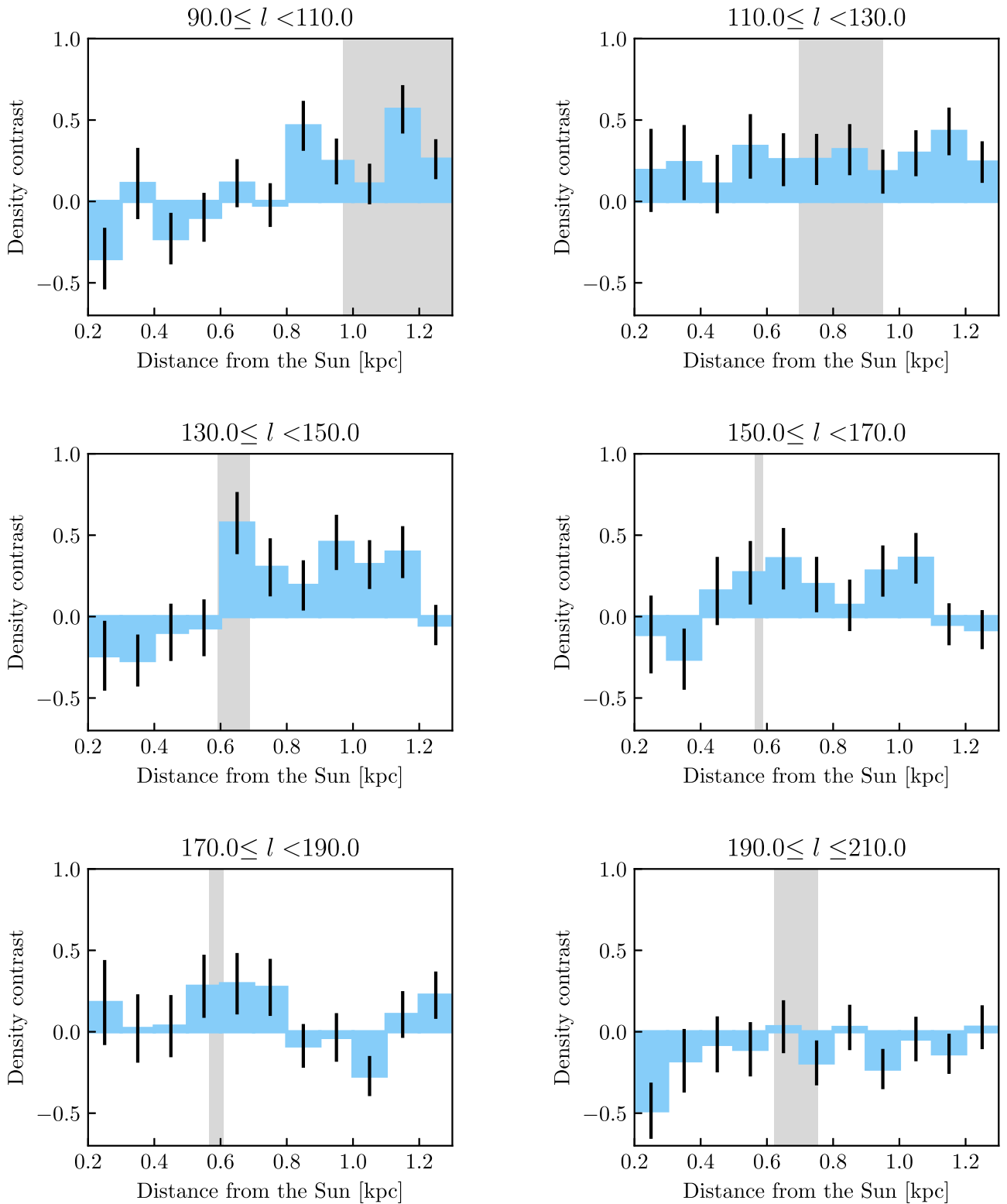
Figure 4. The stellar density contrast as a function of the distance (blue histogram) at the different Galactic longitude ranges as indicated at the top of each panel. The stellar density contrast shown in these panels is the surface density of our sample after division by an exponential profile, as the right panel of Figure 3. The vertical error bars show the uncertainties evaluated by 500 bootstrap sampling. The vertical gray area indicates the distance range of the HMSFR-defined Local Arm as highlighted with the solid black line in Figure 3, in the corresponding Galactic longitude ranges.

than HMSFRs, the offset between HMSFRs, the H$_{II}$ regions, and the stellar arm would provide the strong support for the density-wave scenario.

Lépine et al. (2017) suggested that the Local Arm is caused by trapped orbits at the co-rotation resonance of the major

spiral arms of the Perseus and the Sagittarius–Carina arms. Our stellar overdensity in the similar location to the Local Arm traced by HMSFRs and H$_{II}$ regions does not contradict with this scenario, however, if the offset between these different populations is confirmed to be true, this scenario may be

difficult to explain such offset and different pitch angles for different populations. The stellar Local Arm identified in this paper encourages further quantitative comparison between the model and the observed features.

The offset between the gas and stellar arms is also difficult to explain with the dynamic spiral arm scenario, where no "systematic" offset between the stellar and star-forming arms is expected (Grand et al. 2012a; Baba et al. 2015). On the other hand, the large pitch angle of the Local Arm is consistent with the currently forming spiral arm for the dynamic spiral arm scenario (Baba et al. 2013; Grand et al. 2013). Also, the recent observations of the converging velocity field around the Local Arm (Liu et al. 2017) is consistent with the ongoing formation of the Local Arm. This converging velocity field is different from the diverging velocity field observed around the Perseus arm (Baba et al. 2018; Tchernyshyov et al. 2018). The dynamic spiral arm scenario can explain these differences in the velocity field and pitch angles between the Perseus arm and the Local Arm, if the Perseus arm is in a disrupting phase, while the Local Arm is in a building up phase (Baba et al. 2013, 2018; Grand et al. 2014). However, the dynamic spiral arm scenario has to be able to explain the significant offset found in this paper. The significant external perturbation (see Michtchenko et al. 2019, for an alternative scenario), which is suggested to explain the Galactic disk in-plane and vertical motions found in Gaia DR2 (Antoja et al. 2018; Kawata et al. 2018; Bland-Hawthorn et al. 2019), may affect the origin of the spiral arm in the Milky Way (Laporte et al. 2019), and may be able to explain this offset. Further modeling of the spiral arms including the external perturbations of the Galactic disk is necessary to further understand the formation mechanism of the spiral arm.

Unfortunately, the edge of the stellar Local spiral arm is close to our distance limit. Although we carefully take into account the completeness of the *Gaia* DR2 data, further studies with better data (also taking into account the selection function (e.g., Bovy 2017)) are required to accurately map the Local Arm and the other spiral arm at the farther distances, and answer the long-standing challenge of understanding the origin of the spiral arms in the Milky Way. The result of this paper provides a new and complex picture of the Local Arm, and encourages such further work. The expected parallax accuracy for the fainter stars in the next *Gaia* data releases will certainly help to map the stellar density structures for the different age populations. Ultimately, near-infrared astrometry missions, like the *small-JASMINE* (Gouda 2012), and the *Gaia NIR* concept missions (Hobbs et al. 2016) would be required to answer the structure and origin of the spiral arms.

ORCID iDs

Daisuke Kawata ⓘ https://orcid.org/0000-0001-8993-101X
Mareki Honma ⓘ https://orcid.org/0000-0003-4058-9000

References

Antoja, T., Helmi, A., Romero-Gómez, M., et al. 2018, Natur, 561, 360
Baba, J. 2015, MNRAS, 454, 2954
Baba, J., Asaki, Y., Makino, J., et al. 2009, ApJ, 706, 471
Baba, J., Kawata, D., Matsunaga, N., Grand, R. J. J., & Hunt, J. A. S. 2018, ApJL, 853, L23
Baba, J., Morokuma-Matsui, K., & Egusa, F. 2015, PASJ, 67, L4
Baba, J., Saitoh, T. R., & Wada, K. 2013, ApJ, 763, 46
Becker, W., & Fenkart, R. B. 1970, in IAU Symp. 38, The Spiral Structure of our Galaxy, ed. W. Becker & G. I. Kontopoulos (Dordrecht: Reidel), 205
Benjamin, R. A. 2008, in ASP Conf. Ser. 387, Massive Star Formation: Observations Confront Theory, ed. H. Beuther, H. Linz, & T. Henning (San Francisco, CA: ASP), 375
Benjamin, R. A., Churchwell, E., Babler, B. L., et al. 2005, ApJL, 630, L149
Bennett, M., & Bovy, J. 2019, MNRAS, 482, 1417
Bertin, G., & Lin, C. C. 1996, Spiral Structure in Galaxies a Density Wave Theory (Cambridge, MA: MIT Press)
Bland-Hawthorn, J., & Gerhard, O. 2016, ARA&A, 54, 529
Bland-Hawthorn, J., Sharma, S., Tepper-Garcia, T., et al. 2019, MNRAS, 486, 1167
Bok, B. J. 1959, Obs, 79, 58
Bok, B. J., Hine, A. A., & Miller, E. W. 1970, in IAU Symp. 38, The Spiral Structure of our Galaxy, ed. W. Becker & G. I. Kontopoulos (Dordrecht: Reidel), 246
Bovy, J. 2017, MNRAS, 470, 1360
Bovy, J., Rix, H.-W., Green, G. M., Schlafly, E. F., & Finkbeiner, D. P. 2016, ApJ, 818, 130
Bressan, A., Marigo, P., Girardi, L., et al. 2012, MNRAS, 427, 127
Churchwell, E., Babler, B. L., Meade, M. R., et al. 2009, PASP, 121, 213
Cropper, M., Katz, D., Sartoretti, P., et al. 2018, A&A, 616, A5
Dobbs, C., & Baba, J. 2014, PASA, 31, e035
Dobbs, C. L., & Pringle, J. E. 2010, MNRAS, 409, 396
D'Onghia, E., Vogelsberger, M., & Hernquist, L. 2013, ApJ, 766, 34
Drimmel, R. 2000, A&A, 358, L13
Egusa, F., Mentuch Cooper, E., Koda, J., & Baba, J. 2017, MNRAS, 465, 460
Foster, T., & Brunt, C. M. 2015, AJ, 150, 147
Fujii, M. S., Baba, J., Saitoh, T. R., et al. 2011, ApJ, 730, 109
Fujimoto, M. 1968, in IAU Symp. 29, Non-stable Phenomena in Galaxies, ed. A. Arakelyan (Cambridge: Cambridge Univ. Press), 453
Gaia Collaboration, Brown, A. G. A., Vallenari, A., et al. 2018, A&A, 616, A1
Gaia Collaboration, Prusti, T., de Bruijne, J. H. J., et al. 2016, A&A, 595, A1
Georgelin, Y. M., & Georgelin, Y. P. 1976, A&A, 49, 57
Gittins, D. M., & Clarke, C. J. 2004, MNRAS, 349, 909
Gouda, N. 2012, in ASP Conf. Ser. 458, Galactic Archaeology: Near-Field Cosmology and the Formation of the Milky Way, ed. W. Aoki et al. (San Francisco, CA: ASP), 417
Grand, R. J. J., Kawata, D., & Cropper, M. 2012a, MNRAS, 426, 167
Grand, R. J. J., Kawata, D., & Cropper, M. 2012b, MNRAS, 421, 1529
Grand, R. J. J., Kawata, D., & Cropper, M. 2013, A&A, 553, A77
Grand, R. J. J., Kawata, D., & Cropper, M. 2014, MNRAS, 439, 623
Gum, C. S. 1955, MmRAS, 67, 155

Hobbs, D., Høg, E., Mora, A., et al. 2016, arXiv:1609.07325
Honig, Z. N., & Reid, M. J. 2015, ApJ, 800, 53
Honma, M., Nagayama, T., Ando, K., et al. 2012, PASJ, 64, 136
Hou, L. G., & Han, J. L. 2014, A&A, 569, A125
Hou, L. G., Han, J. L., & Shi, W. B. 2009, A&A, 499, 473
Kawata, D., Baba, J., Ciucǎ, I., et al. 2018, MNRAS, 479, L108
Kawata, D., Hunt, J. A. S., Grand, R. J. J., Pasetto, S., & Cropper, M. 2014, MNRAS, 443, 2757
Kerr, F. J. 1970, in IAU Symp. 38, The Spiral Structure of our Galaxy, ed. W. Becker & G. I. Kontopoulos (Dordrecht: Reidel), 95
Kerr, F. J., & Kerr, M. 1970, ApL, 6, 175
Laporte, C. F. P., Minchev, I., Johnston, K. V., & Gómez, F. A. 2019, MNRAS, 485, 3134
Lépine, J. R. D., Michtchenko, T. A., Barros, D. A., & Vieira, R. S. S. 2017, ApJ, 843, 48
Lin, C. C., & Shu, F. H. 1964, ApJ, 140, 646
Lin, C. C., & Shu, F. H. 1966, PNAS, 55, 229
Lindegren, L., Hernández, J., Bombrun, A., et al. 2018, A&A, 616, A2
Liu, C., Wang, Y.-G., Shen, J., et al. 2017, ApJL, 835, L18
Marigo, P., Girardi, L., Bressan, A., et al. 2017, ApJ, 835, 77
Marrese, P. M., Marinoni, S., Fabrizio, M., & Altavilla, G. 2019, A&A, 621, A144
Michtchenko, T. A., Barros, D. A., Pérez-Villegas, A., & Lépine, J. R. D. 2019, ApJ, 876, 36
Monguió, M., Grosbøl, P., & Figueras, F. 2015, A&A, 577, A142

Morgan, W. W., Sharpless, S., & Osterbrock, D. 1952, AJ, 57, 3
Morgan, W. W., Whitford, A. E., & Code, A. D. 1953, ApJ, 118, 318
Oort, J. H., Kerr, F. J., & Westerhout, G. 1958, MNRAS, 118, 379
Oort, J. H., & Muller, C. A. 1952, MNSSJ, 11, 65
Paladini, R., Davies, R. D., & De Zotti, G. 2004, MNRAS, 347, 237
Pour-Imani, H., Kennefick, D., Kennefick, J., et al. 2016, ApJL, 827, L2
Reid, M. J., & Honma, M. 2014, ARA&A, 52, 339
Reid, M. J., Menten, K. M., Brunthaler, A., et al. 2014, ApJ, 783, 130
Reid, M. J., Menten, K. M., Zheng, X. W., et al. 2009, ApJ, 700, 137
Roberts, W. W. 1969, ApJ, 158, 123
Russeil, D. 2003, A&A, 397, 133
Russeil, D., Adami, C., & Georgelin, Y. M. 2007, A&A, 470, 161
Sellwood, J. A., & Carlberg, R. G. 1984, ApJ, 282, 61
Skrutskie, M. F., Cutri, R. M., Stiening, R., et al. 2006, AJ, 131, 1163
Soubiran, C., Jasniewicz, G., Chemin, L., et al. 2018, A&A, 616, A7
Tchernyshyov, K., Peek, J. E. G., & Zasowski, G. 2018, AJ, 156, 248
Vallée, J. P. 2017, AstRv, 13, 113
Vallée, J. P. 2018, ApJ, 863, 52
van de Hulst, H. C., Muller, C. A., & Oort, J. H. 1954, BAN, 12, 117
Wada, K., Baba, J., & Saitoh, T. R. 2011, ApJ, 735, 1
Walraven, T., Muller, A. B., & Oosterhoff, P. T. 1958, BAN, 14, 81
Xu, Y., Bian, S. B., Reid, M. J., et al. 2018a, A&A, 616, L15
Xu, Y., Hou, L.-G., & Wu, Y.-W. 2018b, RAA, 18, 146
Xu, Y., Li, J. J., Reid, M. J., et al. 2013, ApJ, 769, 15
Xu, Y., Reid, M., Dame, T., et al. 2016, SciA, 2, e1600878